Dynamic motion monitoring of a 3.6 km long steel rod in a borehole during cold-water injection with distributed fiber-optic sensing

Martin Peter Lipus[1], Felix Schölderle[2], Thomas Reinsch[3,1], Christopher Wollin[1], Charlotte Krawczyk[1,4], Daniela Pfrang[2], Kai Zosseder[2]

[1] GFZ German Research Centre for Geosciences, Telegrafenberg, 14473 Potsdam, Germany
[2] Technical University Munich, Hydrogeology and Geothermal Energy, Arcisstr. 21, 80333 Munich, Germany
[3] present address: Fraunhofer IEG, Fraunhofer Research Institution for Energy Infrastructures and Geothermal Systems IEG, Am Hochschulcampus 1 IEG, 44801 Bochum, Germany
[4] Technical University (TU) Berlin, Institute for Applied Geosciences, Ernst-Reuter-Platz 1, 10587 Berlin, Germany

Correspondence: Martin Peter Lipus (mlipus@gfz-potsdam.de)

Abstract

Fiber-optic distributed acoustic sensing (DAS) data finds many applications in wellbore monitoring such as e.g. flow monitoring, formation evaluation, and well integrity studies. For horizontal or highly deviated wells, wellbore fiber-optic installations can be conducted by mounting the sensing cable to a rigid structure (casing/tubing) which allows for a controlled landing of the cable. We analyze a cold-water injection phase in a geothermal well with a 3.6 km long fiber-optic installation mounted to a ¾" sucker-rod by using both DAS and distributed temperature sensing (DTS) data. During cold-water injection, we observe distinct vibrational events (shock waves) which originate in the reservoir interval and migrate up- and downwards. We use temperature differences from the DTS data to determine the theoretical thermal contraction and integrated DAS data to estimate the actual deformation of the rod construction. The results suggest that the rod experiences thermal stresses along the installation length – partly in the compressional and partly in the extensional regime. We find strong evidence that the observed vibrational events originate from the release of the thermal stresses when the friction of the rod against the borehole wall is overcome. Within this study, we show the influence of temperature changes on the acquisition of distributed acoustic/strain sensing data along a fiber-optic cable suspended along a rigid but freely hanging rod. We show that observed vibrational events do not necessarily originate from induced seismicity in the reservoir, but instead, can originate from stick-slip behavior of the rod construction that holds the measurement equipment.

1. Introduction

Fiber-optic distributed sensing in bore-hole applications has gained a lot of attention in the recent years. Distributed temperature sensing (DTS) has been used to assess rock thermal properties and locations of water-bearing fractures (e.g. *Hurtig, 1994*, *Förster, 1997*). DTS was used to perform cement job evaluations and wellbore integrity analysis during and after production tests (e.g. *Pearce et al., 2009*, *Bücker and Großwig, 2017*). The performance of a borehole heat exchanger was monitored with DTS to evaluate the heat input along the wellbore and to measure the regeneration time after a heat extraction period (*Storch et al., 2010*). While DTS has found its way as a standard tool for wellbore monitoring over the last two decades, the utilization of distributed acoustic sensing (DAS) is still subject to many research questions. *Johannessen et al., 2012* introduced the potential and capabilities for acoustic in-well monitoring applications based on DAS systems which range from e.g. flow measurements, sand detection, gas breakthrough, leak detection to vertical seismic profiling (VSP). *Daley et al., 2013*, *Mateeva et al., 2014*, *Harris et al., 2016*, *Daley et al., 2016* and *Henninges et al., 2021* compare traditional geophone with DAS recordings acquired during a vertical seismic profiling campaign (VSP). *Götz et al., 2018* report on a multi-well VSP campaign at a carbon dioxide storage site by using only one single DAS interrogator. *Finfer et al., 2014* performed an experiment to study DAS applications for turbulent single-phase water flow monitoring in a steel pipe. *Bruno et al., 2018* investigate the potential to use downhole DAS data for cross-hole monitoring between two adjacent wells by inducing low frequency pressure pulses to detect high conductivity zones by measuring characteristic vertical strain patterns. *Naldrett et al., 2018* compare fiber-optic technology to traditional production logging tools and provides field data examples of flow monitoring based on both DTS and DAS with wireline-type installations. *Ghahfarokhi et al., 2019* analyze an extensive data set including borehole geophone and DAS during hydraulic fracturing (cable behind casing) to study micro-seismicity and low frequency events in the

borehole. *Raab et al., 2019* shows that DAS data from a behind casing installation can be correlated to conventional cement-bond-long (CBL) recordings by analyzing the acoustic data in noisy drilling and testing operations. *Chang et al., 2020* and *Martuganova et al., 2021* report on reverberating signals in DAS recordings which can occur on free-hanging cables in geothermal wells during fluid injection and which are probably caused by bad cable-to-well coupling. In all reported cases, the coupling of the sensing glass fiber to the surrounding media plays a crucial role for the application of DAS technology.

Especially for the monitoring of deformations occurring over longer time periods, i.e. from minutes to hours to days, the coupling of cable and surrounding environment becomes essential to derive any meaningful result from fiber-optic strain sensing. Where as *Reinsch et al., 2017* provide a theoretical approach to describe the response of the sensing fiber in dependence of the specific cable design, the coupling of the cable to the rock formation strongly depends on the specifics of a measuring experiment. *Lipus et al., 2018* compare data from fiber-optic strain sensing and data from conventional gamma-gamma-density wire-line log during a gravel packing operation in a shallow well for heat storage. *Sun et al., 2020* demonstrate with a laboratory and field test that the extent of a deformed reservoir sandstone and silt caprock by injected CO_2 can be quantitively evaluated using static distributed strain sensing over periods of 42 hours (cable behind casing). *Zhang et al., 2020* provide an attempt to use distributed strain sensing to monitor elastic rock deformation during borehole aquifer testing to derive hydraulic parameter information. *Miller et at., 2018* compare DTS and time-integrated DAS recordings from a borehole and finds a correlation between DTS recordings and very low frequent DAS strain recordings. In their work, they report on repeating "slip events" seen in the DAS data as short and confined vibrational events upon temperature changes in the well.

The study at hand observes similar "slip events" and shows their causal connection to the thermo-mechanical response of the borehole construction to water flow therein.

Installing a fiber-optic cable in a borehole requires specialized equipment. Depending on the aim of the fiber-optic monitoring campaign, different cable installation types are possible. One way is to permanently install the cable by mounting it to the outside of a casing and run it together with the casing into the well and cement it in place (e.g. *Henninges et al. 2005*, *Reinsch et al., 2013*, *Lipus et al., 2021*). A cemented fiber-optic cable generally provides a thorough mechanical coupling to the surrounding structure which is favorable for DAS data quality. Due to its placement behind the casing, the fibers do not interfere with well operations and monitoring of the well can be performed at any time. However, the cemented annulus of a well is a crucial secondary barrier element for well integrity which is compromised by the installation of a fiber-optic cable. A fluid pathway could potentially be created along the cable. cases where the well completion design includes liner elements, a permanent cable installation behind casing to the end of the well is technically not possible, or at least, very challenging. In such cases, other installation types are available. A semi-permanent installation along e.g. a production tubing or a temporary installation via a wireline cable or coiled tubing allow cable placements inside the borehole after drilling is finished. *Munn et al., 2017* present a field test of a novel "flexible borehole coupling technique" that allows deploying fiber-optic cables in boreholes after completion has finished with an improved mechanical coupling compared to lose installed fiber-optic cables. Due to physical constrains, this technology is best suited for shallow boreholes (< 425 m). *Becker et al. 2017* provide an analysis of borehole fracture displacements using such kind of cable coupling technique. Another method to land a fiber-optic cable into a well is by mounting it to a rigid rod (e.g. a pump sucker-rod). The stiff sucker-rod acts as a centralizer and guides the flexible fiber preventing it from coiling up. Such type of installation is especially advantageous when the cable should be placed in a deep and deviated well.

To utilize acquired fiber-optic data from a free-hanging/free-lying rod with the highest possible confidence, it is important to understand the behavior of such a long and stiff structure inside a well. Heating and/or cooling of the well will lead to thermal stresses in the material which potentially result in contraction or expansion of the sucker-rod and fiber-optic cable construction. As the fiber-optic cable is firmly attached to the rods, these dynamics influence the distributed strain and temperature sensing. From DTS monitoring, *Schölderle et al., 2021* found that measurement equipment in the previously described setting does indeed contract upon the injection of cold water and that the points spatially sampled by the distributed sensing change their position. Besides a detailed analysis based on DAS and DTS data of the rod's dynamics in response to temperature changes during a cold-water injection, we show that the resulting thermal stresses are released by the observed vibrational events thus indicating stick-slip like behavior of the rod-borehole wall compound.

1.1 Well description and cable installation

The fiber-optic cable is installed within a production well at the geothermal site Schäftlarnstraße in Munich, Germany. A detailed description of the geothermal site and the cable installation procedure is presented in *Schölderle et al., 2021*. The well was completed with a 20" anchor casing, a 13 3/8", a 9 5/8" liner and a perforated 7" production liner. An overview of the landing depths is presented in Table 1. The design of the borehole completion is schematically shown in Figure 3 (right subplot). The well is vertical to a depth of 250 m. Below 250 m, the well is slightly inclined to 4° down to a depth of 879 m TVD (880 m MD). A number of kick-off-points (KOP) are located along the well path. These are also listed in Table 2. In the result section, a survey shows the well path. From a flow-meter log it is known, that the most prominent feed zone in the well is just below the transition from 9 5/8" liner to 7" perforated liner in the depth interval between 2825 - 2835 m MD.

Table 1: Well design at geothermal site Schäftlarnstraße, Munich (see also Figure 3)

Drill bit Ø	Type	Casing/liner Ø	Top (TVD / MD) [m]	Bottom (TVD / MD) [m]
	Stand-pipe	30"	surface	59.1 / 59.1
26"	Anchor casing	20"	surface	866.2 / 867.5
17 ½"	Liner	13 3/8"	766.0 / 767.0	1812.3 / 2010.0
12 ¼"	Liner	9 5/8"	1740.0 / 1907.2	2408.7 / 2819.0
8 ½"	Perforated liner	7"	2412.2 / 2810.1	2932.7 / 3716.0

	KOP	Inclination [°]	Depth (TVD / MD) [m]	Direction [°]
	#1	44	879 / 880	287
	#2	42	1819 / 2220	250
	#3	58	2432 / 2850	250
	#4	57	2775 / 3432	231

The downhole fiber-optic cable is a tubing-encapsulated-fiber (TEF) that contains two multi-mode and two single-mode fibers. In this fiber-in-metal-tube (FIMT) construction, the sensing fibers are embedded in gel and placed in a metal tube. At elevated strain levels, the gel deforms plastically and allows for a relative motion between fiber and cable. Also, creep between cable construction and optical fibers can occur. Strain measurements with such a type of cable are typically applicable for dynamic strain changes (high frequencies) and low deformations (*Reinsch et.al, 2017*). For longer periods and higher deformations, fiber-optic strain sensing with FIMT cables is still possible but it becomes less localized due to deformation of the material. A laboratory experiment on the relative motion between cable structure and optical fiber in a FIMT cable at higher mechanical stress over time is presented in literature (*Lipus et al., 2018*). The cable has a total nominal diameter of 0.43 inch (1.1 cm) and the cable mantle is made of polypropylene. The cable was landed in the well after drilling was finished. To safely and effectively navigate the placement of the fiber-optic cable down to the end of the almost 3.6 km long well, the cable was strapped to steel rods (sucker rods) which were installed in the well together with the cable. The steel sucker rod also helps to retrieve the cable from the bore-hole when needed. Due to the high deviations in the well at depth, the cable needs to be gently pushed into the well. Therefore, the rigid sucker rod is used for the installation instead of a wireline-type installation. The final landing depth of the sucker rod construction is 3691 m (MD). Figure 1 depicts the configuration of the sucker rod/fiber-optic compound. Together with a number of cross-over elements and the final landing joint, more than 400 of individual sucker rod elements were installed in the well. In the following, we refer to the sucker rod / fiber-optic cable construction as "the rod". The depth reference for the DTS (spot warming) and DAS (tap test) are set to surface.

A fiber-optic pressure/temperature (p/T) gauge was installed with the rod and positioned at the top of the reservoir section at 2755 m (MD).

1.2 Monitoring campaign

149 The data shown in this study was measured before and during a cold-water injection test in a geothermal well.
150 Before the start of fluid injection, the well was shut-in for 29 days, so that the initial temperature profile is close
151 to the natural geothermal gradient of the Bavarian Molasse basin (see *Schölderle et al., 2021*). The temperature at
152 the well head was 17 °C and increasing up to 110 °C at the bottom of the well just before the injection start (see
153 profile "00:48" in left panel in Figure 4). Cold-water fluid injection started on January 23, 2020 at 00:56 by
154 pumping water through the wellhead which leads to a cooling of the well. With an initial water table at a depth of
155 170m below surface, water was injected from the surface without pressure built-up at the wellhead. The cold-water
156 injection was maintained for 24h at a flow rate of 83 m3/h. In this study, we analyze the transient phase of well
157 temperature change for the first 72 minutes of cold-water fluid injection.
158

160 Figure 1: Down-hole cable configuration of the sucker rod with a centralizer (black) and the fiber-optic cable
161 (yellow)

162
163 **2. Data Analysis**
164
165 The analysis in this study is based on the comparison of strain derived from fiber-optic distributed temperature
166 sensing (DTS) on the one hand and distributed acoustic sensing (DAS) on the other.
167
168 **2.1 Derivation of strain from DTS**
169
170 DTS uses each location of a glass fiber as a sensor for temperature (*Hartog, 1983, Hartog and Gamble, 1991*).
171 This is achieved by coupling laser-light pulses into a glass fiber and analyzing the Raman spectrum of the
172 backscattered light whose origin along the fiber is determined by the two-way travel time of the light. In this study,
173 we use a system based on Raman backscatter. Temperature profiles were acquired every 10 minutes with a spatial
174 sampling of 0.25 m. Detailed information about the performance of the fiber-optic system and the calibration
175 procedure are presented in *Schölderle et al., 2021*.
176 We calculate the change in temperature from DTS at the start of fluid injection and the profile later during fluid
177 injection. From DTS measurements we may predict thermo-mechanical deformation according to
178 $$\varepsilon_{DTS}(x) = \alpha_{rod} \cdot \Delta T(x) \qquad (1)$$
179 where α_{rod} is the thermal expansion coefficient and $\Delta T(x)$ is the temperature difference at two subsequent points
180 in time at some location x of the fiber. The rod construction as a whole consists of many different materials with
181 different thermal expansion coefficients, such as the sensing fibers, gel filling, metal tubes, polypropylene mantle,
182 steel rod and nylon centralizers. However, the steel of the sucker rod and the steel of the fiber-optic mantle are the
183 dominant material by weight and the most relevant for any thermal stresses. The sucker rod consists of 4332 SRX
184 Nickel Chromium Molybdenum steel with a thermal expansion coefficient of 10 - 13 µε/K (*Hidnert, 1931*) and a
185 modulus of elasticity of 200 GPa (*T.E. Toolbox, 2012*). The second most dominant material is the polypropylene
186 cable mantle with a modulus of elasticity of 1.5-2 GPa (*T.E. Toolbox, 2012*). The proportion of steel on the thermal
187 stresses in the rod construction are 99.8%. For simplicity, we assume that thermal expansion coefficient $\alpha_{rod} = 13$
188 µε/K for the sucker rod / fiber-optic cable construction and neglect the other materials.
189 **2.2 Direct measurement of strain via DAS**
190 Similar to DTS, DAS also analyzes the back scatter of light coupled into a fiber from one end. Upon contraction
191 or dilatation, the strain-rate of the fiber, i.e. the temporal derivative of relative change of length, can be derived
192 from the temporal change of the interference pattern of coherent light elastically scattered (Rayleigh scattering)

4

from adjacent points within a certain interval of fiber called the gauge length (*Masoudi et al., 2013*). The centroid of the gauge length is defined as a sensor node. The location (x) of a sensor node along the fiber is again determined by the two-way travel time of light from its source to the node and back. In our study, DAS data is acquired at 10000 Hz and down-sampled to 1000 Hz. The gauge length and spatial samping are 10 m and 1 m, respectively. No additional filtering was applied in post-processing (no high pass and no low pass filtering).

In contrast to DTS, DAS directly yields the temporal derivative of strain. In order to convert the measured strain rate $\dot{\varepsilon}$(x,t) data to strain $\varepsilon_{DAS}(x)$ at each location, we integrate in time:

$$\varepsilon_{DAS}(x) = \int_{t1}^{t2} \dot{\varepsilon}(x,t)dt \qquad (2)$$

where t1 and t2 delineate the time window and $\dot{\varepsilon}$(x,t) the recorded strain rate at position x. In the following we speak of "measured strain" ε_{DAS} in contrast to "predicted or expected" strain ε_{DTS}.

We compare ε_{DTS} with ε_{DAS} measurements. We then use the ε_{DTS} data to compute the contractional forces along the rod which occur due to cooling. We compare the result with a static friction curve that was estimated from the sucker rod tally and borehole inclination.

2.3 Stick-slip approach

As the thermal contraction of the cooled sucker rod inflicts a sliding movement of the rods along the borehole wall, we must consider the friction of their relative motion. This friction would yield a stick-slip motion which is observed almost everywhere when two solid objects are moving relative to one another. A detailed review of the origins of stick-slip behavior in mechanical parts as well as an experimental and theoretical analysis on stick-slip characteristics is presented in literature (e.g. *Berman et al., 1995*). In the simplest case, a stick-slip motion appears when the static friction force F_f between two stationary solid bodies is overcome. A schematic drawing of the forces on an interval of the sucker-rod construction at a depth with borehole inclination is presented in Figure 2.
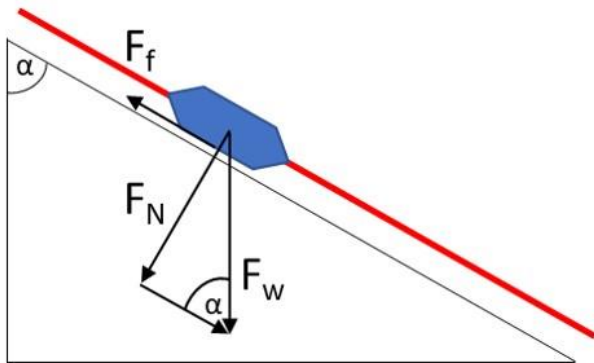
Figure 2: Static friction force F_N and normal force F_N applying on a sucker-rod contact point (nylon centralizer) as a function of the weight force F_w and the borehole inclination 90°-α

The static friction force F_f can be calculated according to

$$F_f = \mu \cdot F_N \qquad (3)$$

where F_n is the normal force and μ the static friction coefficient. The value for μ = 0.36 was obtained from a plate-to-plate experimental analysis on the stick-slip behavior between steel and glass fiber-reinforced nylon specimen (*Muraki et al., 2003*). The force F_N is calculated according to

$$F_N = F_w \cdot sin\alpha = g \cdot m \cdot sin\alpha \qquad (4)$$

where F_w is the gravitational weight force and α the borehole inclination. Each sucker rod element is 9.1 m long, weights 15.7 kg and is equipped with four nylon centralizers and the fiber-optic cable (20 g/m). Therefore, the weight force for each contact point of the rod construction yields F_w = 9.81 m/s^2 * 15.9 kg / 4 = 39.0 N. Regarding the lowermost part of the rod construction as an example, this means that for the last nylon centralizer (borehole inclination of 54°), a static friction force of F_f = 0.36 · 39.0 N · sin (54°) = 11.3 N is calculated. With respect to contraction of an initially unstressed rod construction, for each subsequent nylon centralizer towards the surface,

5

236 the friction force of the rod at the given depth is calculated by the cumulative sum of all friction forces from the
237 nylon centralizers below. The friction force increases with decreasing well depth. Two further weights are added
238 to the friction force profile: the bottom end of the sucker rod is a 1.4 m long steel piece with a weight of 64 kg and
239 the carrier of the pT gauge at 2755 m MD is a 2.2 m long steel piece with a weight of 105 kg. Here, we applied a
240 static friction coefficient for steel on steel of $\mu = 0.8$ (*Lee and Polycarpou, 2007*).

242 The expected thermal contraction ε_{DTS} can also be translated to a force. Assuming a Young's modulus for stainless
243 steel of $E = 200$ GPa (*Cardarelli, 2018*) and given the cross-sectional area of the rod ($A_{rod} = 2.9$ cm^2), we can
244 calculate the applied force F_{app} at each location along the rod which was thermally induced within the investigated
245 one-hour cold-water injection period:

247 $$F_{app} = \sigma \cdot A_{rod} = E \cdot \varepsilon_{DTS} \cdot A_{rod} \qquad (5)$$

249 For simplicity, we assume that the elasticity from the fiber-optic cable and the nylon centralizers are neglectable
250 and that the steel dominates the mechanical behavior of the structure. Furthermore, we make the assumption that
251 no mechanical stresses are exerted on the rod prior to the cold-water injection. This allows us to set a zero-force
252 baseline before injection start for the stick-slip analysis.

254 **2.4 Stick-slip event detection and picking**

256 In the DAS data we monitored repeating vibrational events with ongoing cold-water injection in the deeper part of
257 the well. These events are characterized by a sudden DAS amplitude peak at some depth and an up- and downward
258 directed move-out. With time, the spatio-temporal distribution of these vibrational events changes. To automate
259 the detection of depth location and moveout of an event, we employ a short-term/long-term average trigger (*Allen,*
260 *1978, Vaezi and v.d. Baan (2015))*. The parameters used for the STA/LTA analysis can be found in Table 2:

262 *Table 2: Parameters used for the STA/LTA detection method*

Parameter	Value
STA window length (N_s)	1 s (1000 samples)
LTA window length (N_L)	3 s (3000 samples)
Trigger start threshold τ_1	2
Trigger end threshold τ_2	0.8

266 **3. Results**

267 Figure 3 shows examples of raw and unprocessed strain rate data measured with the DAS unit in the well at the
268 start of cold-water injection (1st subplot), one hour after start of fluid injection (2nd subplot) and shortly after the
269 end of the 24 hours water injection period (3rd subplot). Each subplot depicts 10 seconds of data with the same
270 data color scaling. A number of features can be recognized in each of the data examples. At the depth marked with
271 the arrow "A", there is a transition from a noisy depth interval above to a rather quiet one below. The transition
272 marks the location of the water table in the well. From the wellhead, the water free-falls down to the water table
273 at about 170 m below surface. In the cased hole section down to the depth of the transition to the perforated liner,
274 high velocity tube waves (around 1500 m/s) are present which are reflected at the liner shoe of the 9 5/8" casing
275 at ca. 2810 m MD (arrow "B" in first subplot). Below "B", the cable is located inside the perforated liner. The tube
276 waves are not further guided in this interval and the noise level is rather low. In the uppermost 100 m of the
277 perforated liner section (2810 – 2900 m MD), a strong signal is present in the 2nd and 3rd subplot (arrow "C"). The
278 arrow "D" marks another common characteristic feature in the DAS data which was observed over the analyzed
279 cold-water injection period. This abrupt and localized signal is interpreted as a sudden contraction of the sucker
280 rod.
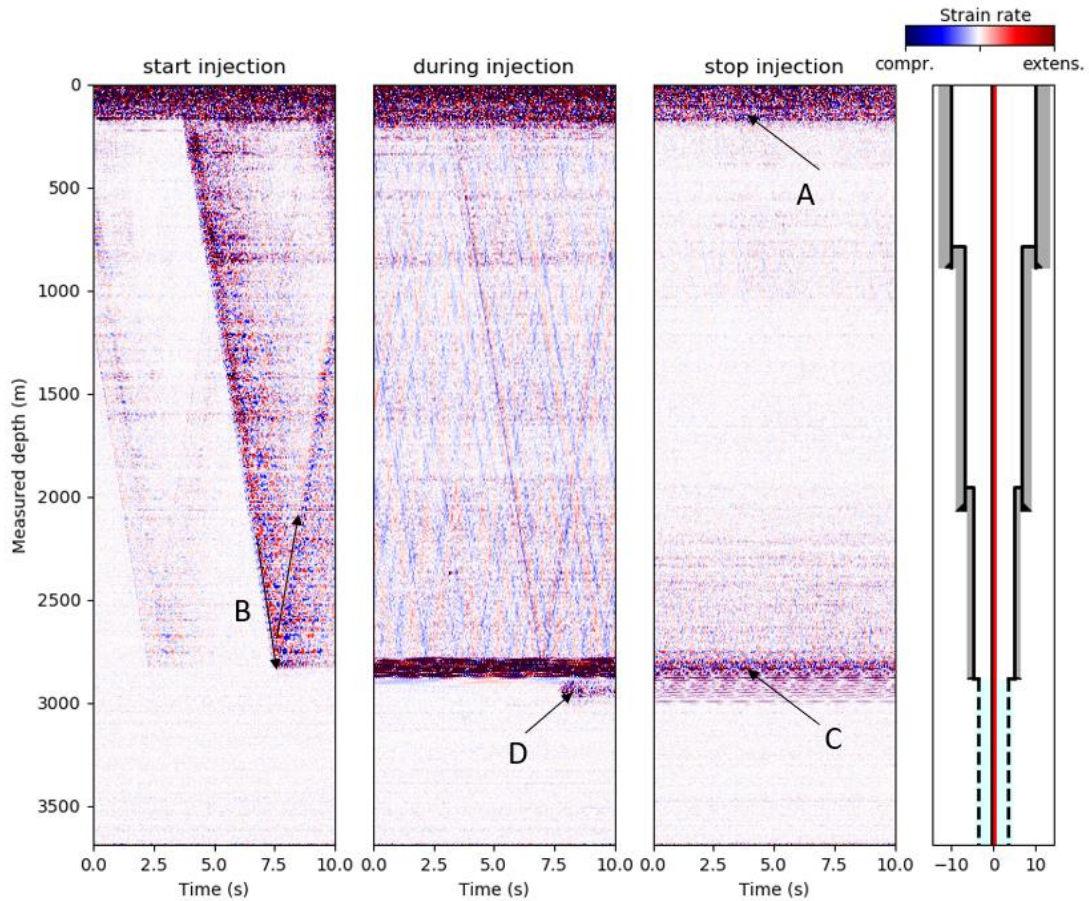
3.1 Sucker rod contraction

Figure 4 shows fiber-optic data from DTS and DAS for the first hour of cold-water fluid injection testing. The first subplot shows three DTS profiles at 00:48, 01:18 and 02:08, which are -8, +22 and +72 minutes relative to the cold-water injection start. The entire rod from surface to 3100 m experiences cooling. Below the most prominent feed zone of the well at 2830 m MD, the cooling of the well decreases. This is because most of the injected cold-water flows into the formation (2825 - 2835 m MD) and the fluid column below remained rather undisturbed. A theoretical tensile strain from thermal contraction of the steel rod (and the fiber-optic cable) ε_{DTS} can be derived from the temperature difference between the two profiles for a certain depth relative to the profile at 00:48. The second subplot compares the 15 m moving average of ε_{DTS} calculated after formula (1) with the local strain (ε_{DAS}) calculated after formula (2) during the same time interval. The third subplot shows the borehole inclination from the deviation survey. On the fourth subplot, a schematic representation of the casing/liner landing depths is shown together with the location of the rod.
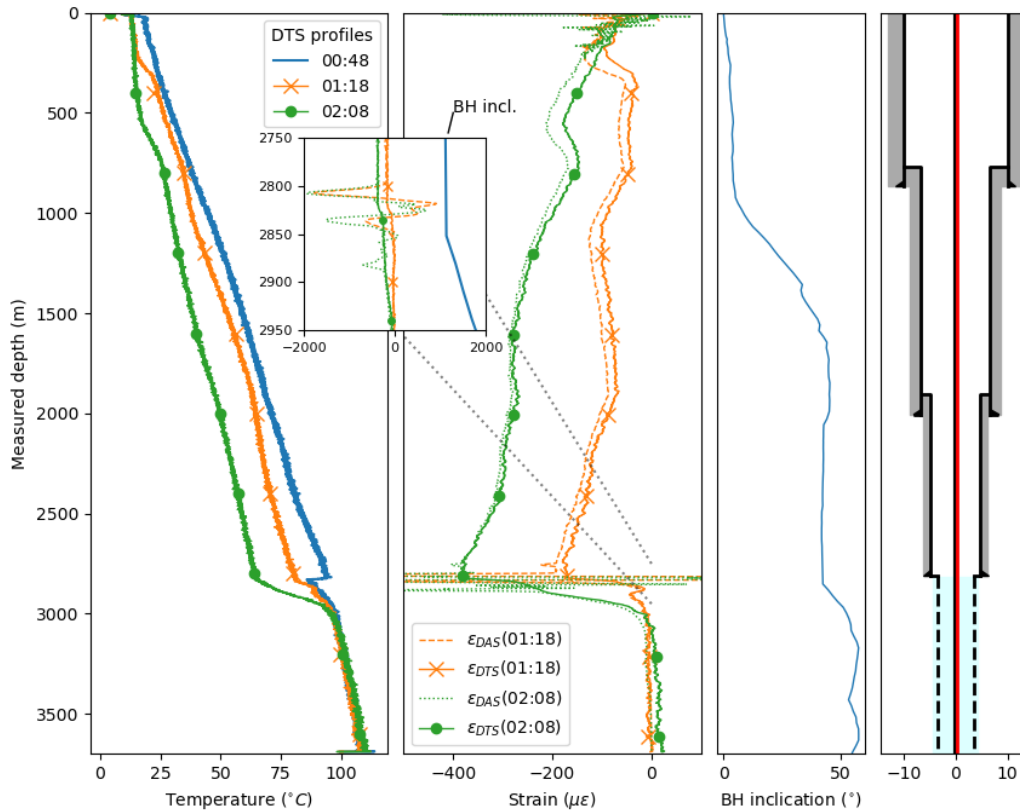
Figure 4: Downhole monitoring data during the cold-water injection test. 1st subplot: DTS temperature profiles. 2nd subplot: Comparison of strain profiles ε_{DTS} and ε_{DAS}. 3rd subplot: borehole inclination. 4th subplot: wellbore schematic

In general, a clear match is visible between ε_{DTS} and ε_{DAS} for the entire well which means that the strain the steel rod experiences (ε_{DAS}) follows the predicted thermal contraction (ε_{DTS}). However, there are depth intervals where the experienced strain (ε_{DAS}) exceeds and others where it falls short on the predicted strain (ε_{DTS}). Until 2825-2835 m MD where the most prominent injection interval is located, ΔT increases with increasing depth. At the injection interval ΔT rapidly increases. Below this zone, no thermal contraction is expected.

Along the 13 3/8" casing interval (from top liner hanger 13 3/8" at 768 m MD to top liner hanger 9 5/8" 2010 m MD), ε_{DTS} and ε_{DAS} are negative and show the same trend thus indicating the expected contraction. In absolute values expected strain ε_{DTS} exceeds the measured strain ε_{DAS}. Over this depth interval, the well inclination increases from nearly vertical to 45°.

At the transition to the 7" perforated liner at 2810 m MD (top liner hanger packer) a notably different ε_{DAS} pattern is measured compared to ε_{DTS} (box plot in Figure 4). In the depth interval 2795-2815 m MD, the expected contraction from ε_{DTS} at 01:18 yields -170 µϵ (-380 µϵ at 02:08), while the estimated contraction from ε_{DAS} at 01:18 results in -1740 µϵ (-1950 µϵ at 02:08) µϵ between 2805-2810 m MD, which is more than a factor 10 higher (factor 5 at 02:08). In the depth interval 2815-2830 m MD, ε_{DAS} shows an extension of the rod with a maximum of 900 µϵ at 01:18 while ε_{DTS} decreases from -160 µϵ at 2815 m MD to -55 µϵ at 2835 m MD. This is the only locations in which the integrated strain rate from ε_{DAS} shows extension instead of the predicted contraction. At 2830-2850 m MD, another interval with extraordinary high ε_{DAS} readings relative to ε_{DTS} is present. Below 2850 m MD, ε_{DAS} and ε_{DTS} again follow the same trend at 01:18. At 02:08, the ε_{DAS} and ε_{DTS} show a discrepancy down to 2890 m MD and the same trend below. The gyro data shows a sudden increase in the inclination of the borehole at 2850 m MD. Between 2900-3100 m MD, the temperature difference between the two DTS profiles rapidly decreases (see Figure 4, 1st and 2nd subplot). At 02:08, the DTS profile shows slightly increased temperatures (+1 °C) with a constant offset from 3100 m to the end of the cable compared to the DTS profile at 01:18. This leads to a constant offset of a positive expected strain εDTS. The measured strain εDAS shows no offset in this depth interval.

3.2 Sudden contraction events

**Event description**

A close-up of raw DAS data is shown for the depth interval 2500-3300 m MD around the transition from cased hole to perforated liner 52 minutes after the start of the cold-water fluid injection (see Figure 5). At this time, the DAS records a transient strain-rate anomaly. Similar events are repeatedly observed in the course of the measurement during the cold-water injection periods. Using the event shown in Figure 5 as a representative example, we describe common features of these events in the following. Its origin lies at 600 ms and 3000 m MD and is characterized by an abrupt increase of the measured strain rate. The sudden increase of strain rate amplitude propagates both up- and downwards along the well with compressional and tensional sign of amplitude, respectively, where the propagation velocity upwards is approximately 3900 m/s (green Line A in Figure 5). In contrast, the downward propagation velocity is slower and shows irregularities from 650-1260 m/s. Most striking is the decay of the velocity from 3200 m MD onwards and the eventual stop of propagation slightly above 3300 m MD. In upward direction, this event is halted somewhere in the noisy interval where the reservoir section of the borehole begins. The event is followed by elastic reverberations that decay after approximately half a second.

Further examples of such kind of events are plotted in Figure 6 A, B, C and D. They all have in common, that they originate below 2900 m MD and trigger a contraction above and an extension below. The previously discussed event is characterized by a smaller precursor 100 ms before the origin of the large event at the same depth. Precursors and successors can also be observed in the examples in Figure 6 (in particular in Figure 6 B), yet the events shown here are distinguished by the fact that their upwards propagation extends beyond the noisy reservoir section. All exemplary events except 6A whose downward propagation arrests rather sudden, have in common that the up- and downwards propagation slow down before coming to a halt. Another striking observation in all of the events is that the initial onset propagates slower than the reverberations in the coda.

While the exact shape of the spatial propagation and length varies (length between 20–1600 m), the duration of these events is mostly in the range of 0.5 s with some fading noise/reverberation afterwards. These events typically show a tensional signal at the energy front in the downward direction while the initial energy front upwards is mostly compressional. As the vibrational signal propagates along the rod, a succession of compressional and tensional waves is created which moves with a velocity of about 3900 m/s along the rod (as shown by the green line A in Figure 5). The downward propagation of the first arrival changes its velocity from the onset of the event towards the end of the vibrational event. In the first 50 ms, it increases in velocity, then it stays constant before it gradually decreases in velocity at around 700 ms below 3200 m MD.

The four black arrows on the left y-axis in Figure 5 indicate the timeseries for which the four spectrograms shown in Figure 7 were calculated with a moving window of 250 ms. The DAS strain-rate timeseries at 3000 and 3200 m MD show the onset of the slip event at 0.5 s with dominant frequencies of the first break between 30 and 75 Hz. The slip only lasts approximately half a second but reverberations of different duration and different frequencies can be observed in band below 30 Hz depending on the rod segment. For instance, at 3000 m MD long lasting reverberations occur at ~10Hz whereas at 3200 m MD they occur at 20 Hz. As can be seen from the spectrogram from the DAS strain-rate recordings at 2700 and 2835 m MD, the slip event does not penetrate into and beyond the feed zone whose characteristic noise at 24 Hz remains undisturbed just as the low frequency pattern of the tube waves above.
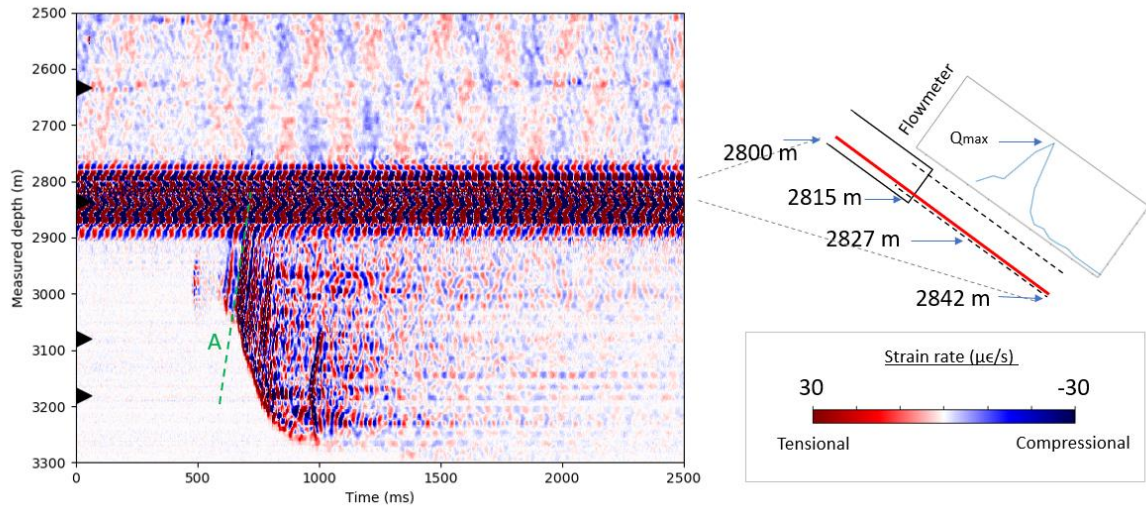
365

366 *Figure 5: Sucker rod contraction event displayed by strain rate DAS data (left). The black arrows on the left y-axis*
367 *mark the depth location of timeseries used for the spectrograms in Figure 7. Line "A" marks the moveout of the*
368 *signal at a speed of 4000 m/s. The schematic drawing shows the inclination of the borehole with the fiber-optic*
369 *cable (red) lying inside of the casing (right). The inflow profile from a wireline flowmeter measurement is shown by*
370 *the blue graph*
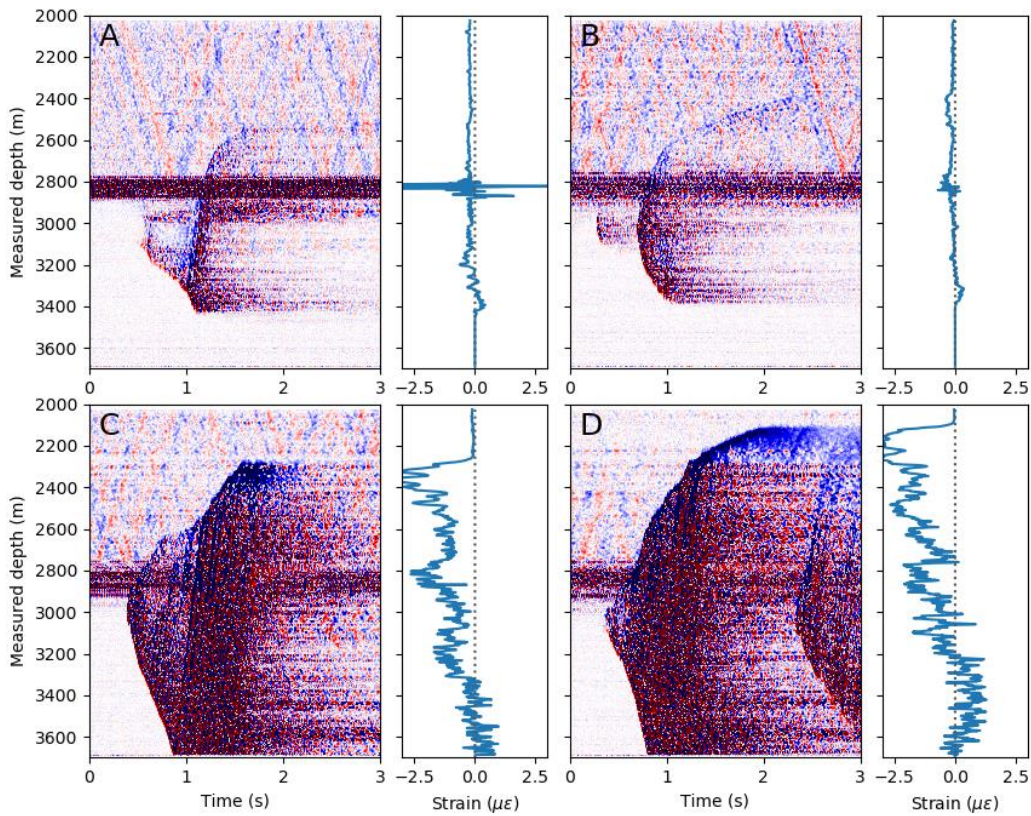
371

372 *Figure 6: Four raw DAS data examples of sucker rod events with the integrated strain rate (ε_{DAS}) over a period of*
373 *3 seconds. The timing of the events relative to the start of cold-water injection is: + 65 minutes B: + 110 minutes*
374 *C: + 147 minutes and D: 210 minutes*

375

10
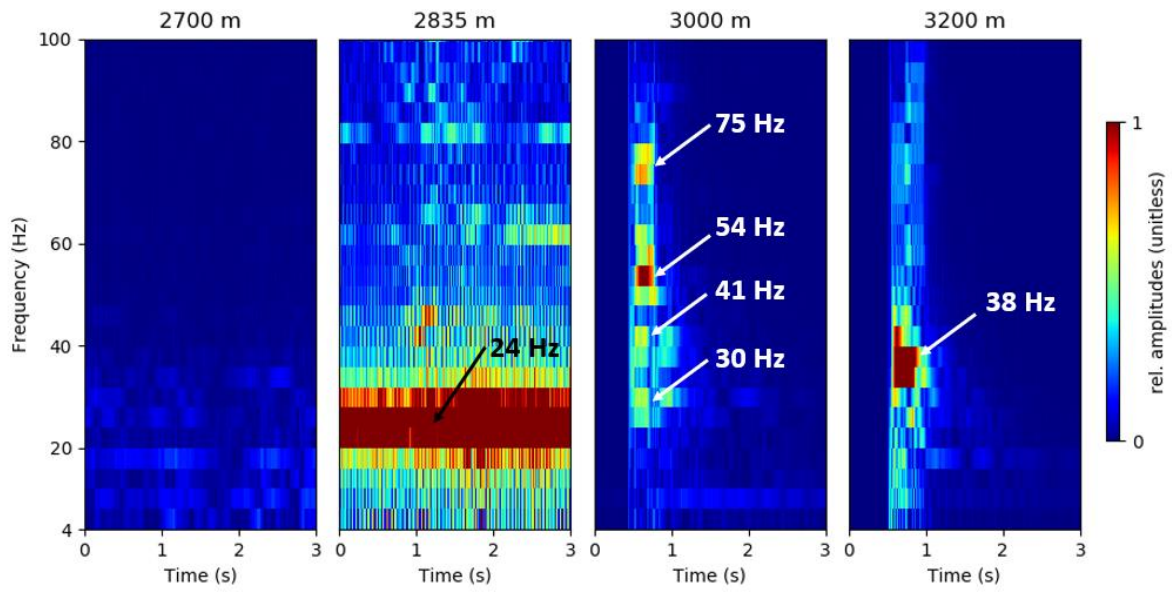
Figure 7: Spectrograms for a 250ms moving window at different depth along the well during the sudden vibrational event depicted in Figure 5. Red colors indicate high amplitudes, blue colors low amplitudes. The relative amplitudes are displayed by the same color ranges for all subplots.

383 **Event detection over time**

384

385 We applied a STA/LTA algorithm to automate the detection of the sudden vibrational events within the first 72
386 minutes of cold-water fluid injection. Three attributes are obtained for each event: a) the depth location where the
387 event starts b) the lower end and c) the upper end of the event according to the STA/LTA algorithm. Figure 8
388 shows one example of the automated detection with the STA/LTA trigger. The upper subplot shows an example
389 trace of raw DAS data at a depth of 3120 m MD (marked by the black arrow in the lower subplot) and the
390 corresponding STA/LTA characteristic function. Beginning and end of the detection are marked by the green and
391 orange crosses, respectively. The lower subplot shows spatio-temporal DAS data and the detection of two
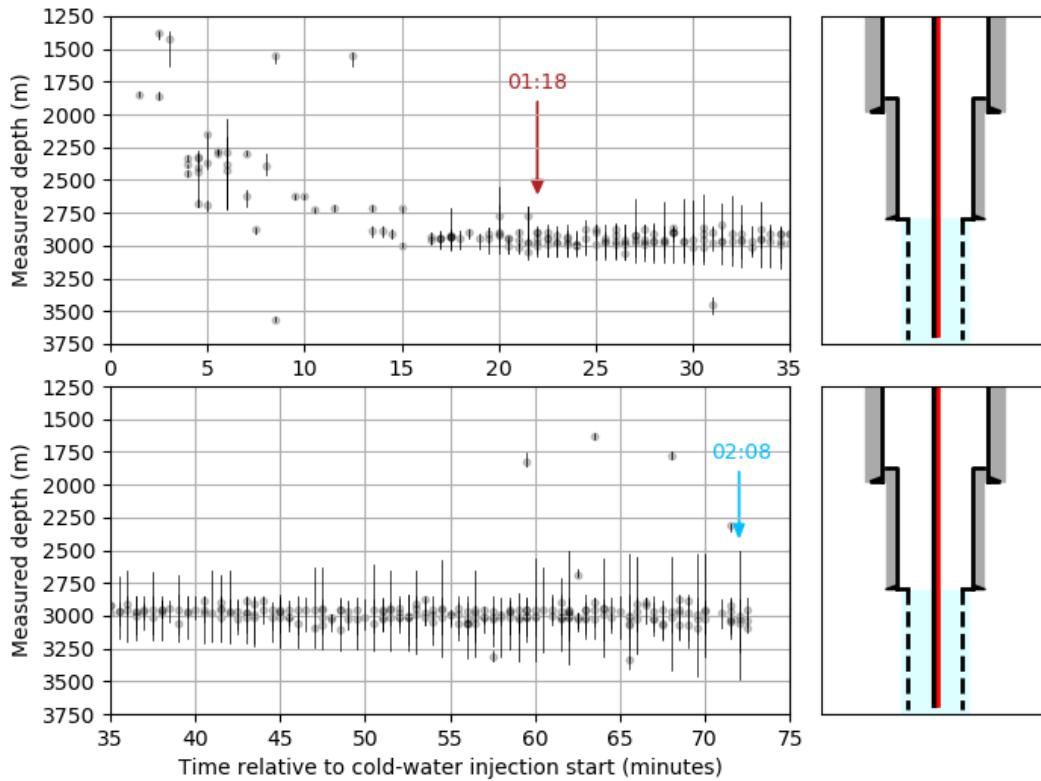392 vibrational events.

393
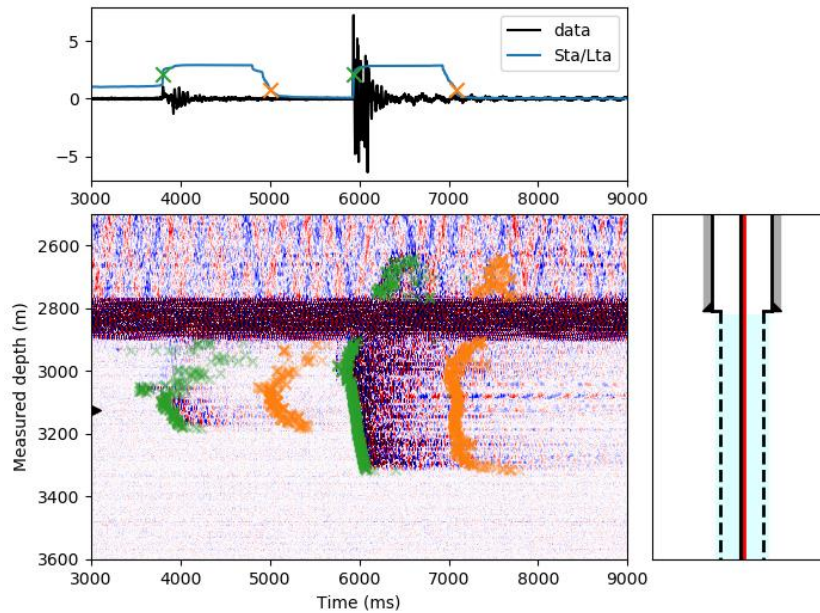
394
395 *Figure 8: STA/LTA trigger algorithm applied as an automated detection method for vibrational events. Trigger*
396 *start and end is marked with green and orange crosses*

397 All vibrational events which occurred within the first 72 minutes of cold-water fluid injection are plotted in Figure
398 9. Gray circles mark the spatio-temporal origin of vibrational events. The corresponding vertical black line
399 indicates the spatial extent of the respective event. In this representation, events with a spatial extent of less than
400 20 m are neglected. Such small events occur between 4-10 times per minute in the depth region from 1250-2750
401 m MD over the entire investigated 72 minutes after fluid injection start. Within the first 15 minutes, only a
402 relatively small number of bigger vibrational events occur, i.e. events which extend over more than 20m. Early
403 events (within the first 5 minutes relative to injection start) appear in the depth region between 1250-1900 m MD.
404 Except for two large events (4 minutes: 2260-2730 m MD and 6 minutes: 2040-2700 m MD), the spatial extent of
405 the vibrational events is rather small. One single event was recorded at a depth of 3540-3580 m MD close to the
406 shoe of the installation. With time, the depth of vibrational events increases to 2900 m MD. From 17 minutes
407 onwards, the occurrence of vibrational events is mostly constrained in the depth region from 2900-3100 m MD.
408 The maximum spatial extent of large vibrational events increases with time. From 01:18 (+22 minutes after
409 injection start) onwards, most of the events extend into the depth region of 2835-3080 m MD. At 02:08 (+72
410 minutes to injection start), the spatial extent of the events is 2500-3470 m MD.

411 With time, the frequency of the occurrence of the events decreases. 4-5 hours after injection start, large events
412 (such as in Figure 6 C and D) appear every 10 – 15 minutes. 8 hours after injection start, large events appear
413 approximately every 25 – 40 minutes.

12

Figure 9: Gray circles and black vertical lines indicate the spatio-temporal origin and spatial extent of vibrational events in the well, respectively. The shown period comprises the first 72 minutes of cold-water fluid injection.

3.3 Friction force model

The static friction force F_f after formula (3) is compared to the applied force from thermal contraction of the rod F_{app} after formula (5) which was evaluated for the period from injection start to 01:18 (+22 minutes after start of injection) and to 02:08 (+72 minutes after start of injection) (Figure 10). The gravitational weight force F_w per nylon centralizer is constant for every contact point of the rod. The force needed to overcome the cumulative static friction F_f is a function of the borehole inclination. F_f increases from the bottom of the rod installation at 3691 m MD towards 1000 m MD. The bottom end of the sucker rod and the carrier of the pT gauge at 2755 m MD create an additional static friction force of 0.4 kN and 0.5 kN, respectively. Above 1000 m MD, the well is nearly vertical and only little static friction is expected. The static friction F_f at 1000 m MD yields 26.1 kN. F_{app} at 01:18 is lower than F_f for the entire installation length. Only in the depth interval 2731-2820 m MD, F_{app} approaches a force of 10.5 kN which is close to F_f. This indicates that forces are sufficient to initiate relative motion between sucker rod and casing at that depth. With ongoing cold-water fluid injection, the applied forces F_{app} increase with further decreasing temperatures. At 02:08, F_{app} surpasses the frictional forces in the depth range from 2150-2912 m MD. F_f and F_{app} intersect at 17.0 kN and 9.3 kN, respectively. At the depth interval from 2732-2820 m MD, the applied force peaks at 22.0 kN (shown in Figure 10). For all estimates given above, it is assumed that the sucker rod did not move relative to the casing, i.e., thermal stresses can build up but will not be released by relative motion.

13
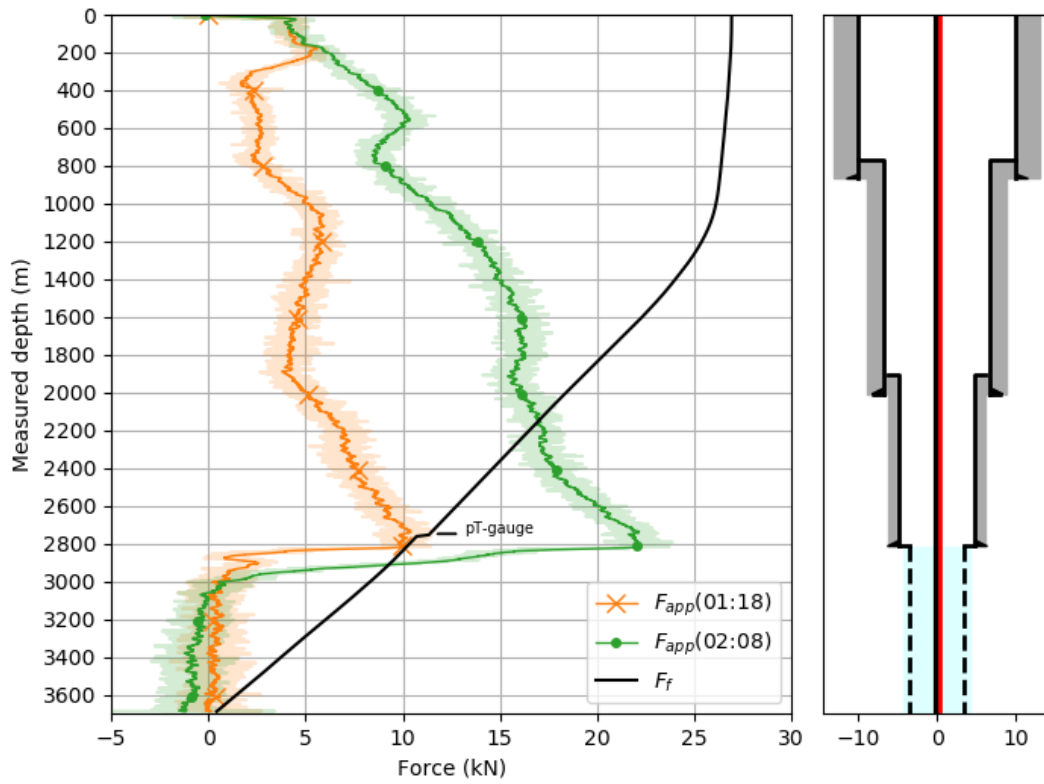
Figure 10: Comparison of static friction F_f with applied forces F_{app} from thermal contraction of the rod within the first 72 minutes of cold-water fluid injection. The pale colors in F_{app} originate from measured DTS data and the solid lines are constructed by a moving average over 15 m

4. Discussion

With the help of distributed fiber-optic temperature and acoustic data, we monitored a cold-water injection period in a geothermal well at the site Schäftlarnstraße, Munich. The downhole monitoring data allows for an analysis of the deformation of the 3.6 km long sucker rod/fiber-optic cable construction due to cooling. We observe numerous localized episodes of large strain-rates that nucleate along the inclined stretch of the borehole and propagate both towards greater depth and the surface. Such events induce quickly declining elastic vibrations along the entire extent of the affected interval. The emergence of these vibrational events strongly correlates with the beginning of the fluid injection. In the following, we thus argue that the vibrational events are a result of the substantial temperature changes which the sucker rods with the optic fiber are exposed to. The contraction of the sucker rods upon cooling induces stress where the sucker rod is held to the borehole wall by frictional forces. On the basis of a simple mechanic model we show that accumulated stresses may eventually exceed the friction giving rise to sudden stress release and the observed strain changes.

4.1 Assessment of measuring errors

Our monitoring data analysis is based on a debatable approach of integrating DAS data over longer time periods. To obtain the ε_{DAS} profile over the period of 1 hour, a total number of 3.6 million strain rate profiles are integrated (sample rate: 1000 Hz). Such kind of numerical operation has a high risk of creating numerical errors due to e.g. rounding off or value truncation. In addition, the smallest systematic error in the DAS measurement system results in a significant drift over time which would misrepresent the strain profile measured by the sensing fiber. Also, it is well known that for FIMT type of installations, the gel filling allows for a creep and differential movement of fibers with respect to its surroundings which makes strain sensing unreliable for greater deformations and longer periods (e.g. *Lipus et al., 2018*, *Becker et al., 2020*). However, a creep over many meters or even kilometers is most likely improbable. To strengthen the meaningfulness of our integrated strain profile, we analyzed the ε_{DAS} for a deeper section of the well, where little temperature change (ca. 1 °C) was measured by the DTS. In 3500 m depth, we do not observe any strain accumulation after temporal integration of strain rate data over a period of 60 minutes. This indicates that the measured strain rate has no significant drift during the time of interest. For measurements with higher amplitudes such as within the depth interval 2800-2900 m, non-linear effects influencing the temporal integration of the data cannot be excluded.

4.2 DAS data integration

We integrated DAS data in time over 72 minutes to assess the absolute contraction of the rod construction prior to the cold-water injection start (see Figure 4). For the well interval from water table to the transition to the perforated liner, the results show a good match to the contraction that was theoretically assumed from the cooling of the well. However, from 2800-2900 m MD, we obtain much higher deformation from the DAS data than what we expected. We cannot give an unambiguous explanation for that but see two likely reasons for that observation. Firstly, the DAS integration process might result in a drift when integrating high amplitude DAS data. Especially from 2800-2900 m MD, constantly high energy is recorded by the system. The second explanation could be that the integrated DAS data measured a true deformation of the construction. In the depth region around 2800 m, the annular space of the borehole is rather irregular (transition to 7 " liner interval, localized increase in the borehole inclination (see Figure 4, 3rd panel)). The repeating sudden sucker rod events might lead to an uneven distribution of the thermal stresses along the rod. Interestingly, the most prominent feed zone of the well coincides with the one single DAS interval which shows an extensional signal.

The sudden slip events presented in this study show some similarity to the "slip events" which were previously observed in FIMT-type fiber-optic installation in a geothermal well (*Miller et al., 2018*). In the reported DAS campaign, a fiber-optic cable was installed in a geothermal well and it is argued that repeated thermal cycles led to a loss of frictional coupling between fiber-optic cable and the borehole wall. *Miller et al., 2018* reported that a sudden loss triggered a movement of the cable with a first arrival speed of 4600 m/s (we measured a first arrival speed of 4000 m/s). The integrated strain of the reported event shows a balance towards absolute contraction which we also observe in our events. Another similarity is given by the frequency content of these events. They recorded a dominant frequency of 45 Hz with some harmonics in both directions which we also observed in our data (see Figure 7 at 3000 m MD).

4.3 Stick-slip rod behaviour

We calculated the static friction force F_f along the rod construction by a cumulative sum of the friction of each nylon centralizer with the borehole inner wall. Independently of that, we computed the applied force F_{app} on the rod construction by thermal contraction using the DTS monitoring data. By comparing both curves, we can distinguish depth regions where the rod remains immobile ($F_f > F_{app}$) and depth regions where the applied forces overcome the static friction force ($F_f < F_{app}$). The temperature difference in the course of the investigated time period is particularly high over the 9 5/8" liner interval (depth region from 2485-2890 mMD) which in consequence also means that F_{app} is high. According to our model calculation, the contraction forces surpass the frictional forces at 2800 m MD around 01:18 (22 minutes after injection start). This result implies that after this time, the construction can contract in this depth interval. In other words, the thermal stresses on the rod construction in this depth region are high enough that the rod starts to move and to contract. Hence, the literature values assumed for the static friction between sucker rod and steel liner are assumed to approximate the real values.

With ongoing cold-water injection and further cooling of the well, the applied forces F_{app} increase. This leads to a continuous growing of the depth interval where F_{app} surpasses the static friction F_f of the rod. The STA/LTA detections match the predictions of the friction fore model. After a rather quiet initial phase of low energetic events (before 17 minutes in Figure 9) which could be caused by the relaxation of previously accumulated stress anomalies along the sucker rods, repeated vibrational events start to concentrate in the region 2800-3100 m MD. As the region with $F_f < F_{app}$ increases, the length of the vibrational events increases. From our friction force model, we would expect vibrational events (more specifically: the contraction part of the movement) at 02:08 in the depth region 2150-2910 m MD. However, the observed events extend from 2500-3500 m MD. Regarding the upper limit, we can see in Figure 10 that there is a significant change in slope for F_{app} at 02:08 at 2500 m MD. The friction force model is based on numerous assumptions (i.e. static friction coefficient nylon-steel, Young's modulus for stainless steel, neglecting fiber-optic cable, stress-free initial conditions) which might not accurately depict the downhole conditions. This could mean, that either the calculated applied force F_{app} is too high and/or the static friction force F_f is too low.

With respect to the lower limit of the vibrational events, we predict the contraction part (*$F_{app}(02:08)$* Figure 10) of the vibrational events down to a depth of 2912 m MD from our friction force model. However, we record vibrational events down to a depth of 3480 m MD. This discrepancy can partly be explained by the fact that the model prediction only shows the contraction part of the vibrational event. As seen in the cumulative strain *ε_{DAS}* (see Figure 6 event A and B), the lowest part of a vibrational event yields extension. The most likely reason is that the contraction above results in a pulling of the rod from a lower lying region to compensate for the missing rod length. Therefore, the events can be traced down to a greater depth than predicted.

The constant temperature offset by +1 °C in the DTS profiles from 02:08 (relative to 01:18) in the depth interval from 3100 m MD to the end of the cable is unlikely to be caused by any fluid movement. While DTS temperature measurements did show a variation, no additional offset was recorded from the measured strain ε_{DAS}. This could mean that the rod builds up thermal extensional stresses without actual movement taking place ($\varepsilon_{DTS} > 0$ $\varepsilon_{DAS} = 0$). However, we speculate that the temperature anomaly is related to the processing of the DTS data. DTS temperature was measured in a double-ended configuration. A temperature profile is created by overlaying the DTS signal from both directions which are measured consecutively for both fiber branches. Close to the folding location (at the bottom of the well), an asymmetry in the temperature reading was observed between both fiber branches, which does not seem to be caused by any fluid motion. Averaging this difference between both branches led to a temperature offset. This offset was only visible if strong temperature changes were observed.

5. Conclusion

The field test at the geothermal site Schäftlarnstraße demonstrates that simultaneous recording of DTS and DAS data can be used for a detailed analysis of the deformation of a sucker rod type of fiber-optic cable installation in a 3.6 km deep well. By comparing the theoretical contraction of the rod structure from DTS with an estimated contraction from DAS, we can distinguish depth intervals with higher and lower thermal stresses in the material. We introduce a friction force model which accurately predicts the onset and extent of sucker rod events releasing accumulated thermal stress. This is an important finding for DAS monitoring in geothermal settings because it shows that localized high-energetic vibrational events must not necessarily be related to microseismic events

occurring in the rock formation but can originate in the subsurface construction and the way how the fiber-optic monitoring equipment is installed in the well. Moreover, the friction force model is useful to predict the data quality for DAS measurement campaigns for deep sucker-rod types of fiber-optic installations. Especially for the recordings of weak acoustic signals that are e.g. induced by fluid movement in the annulus, it is essential to know the potential sources of errors and artifacts in the data. During operations which introduce a temporal temperature gradient, thermo-mechanical response of freely hanging steel parts in the borehole may introduce stick-slip events that must be distinguished from any other relevant seismogenic source. Potentially, the vibrational energy from the sucker rod events can also be used to study the formation velocity in the near-field around the borehole. Furthermore, the large-scale contraction along certain sucker rod and fiber intervals must be considered with respect to the location of the distributed sensor nodes. Our description also serves as a starting point for a more detailed dynamic description of the observed processes. This can be of use to predict onset and depth interval of such sucker rod events and to contain their destructive potential in case of too quick cooling of the construction.

Code and data availability

Python scripts and data are available upon request to the corresponding author.

Author contributions

TR and KZo conceptualized, planned and coordinated the monitoring campaign. MPL, FS, CW, TR and DP conducted the field measurement. MPL performed the DAS data processing. All authors contributed in the interpretation of the results. MPL prepared the first draft of the manuscript with the contribution from all authors.

Competing interests

The authors declare that they have no conflict of interest.

Special issue statement

This article is part of the special issue "Fibre-optic sensing in Earth sciences". It is not associated with a conference.

Financial support

Acknowledgements

References

Allen, R. V. "Automatic earthquake recognition and timing from single traces." *Bulletin of the Seismological Society of America*, 1978.

Becker, M. W., C. Ciervo, M. Cole, T. Coleman, and M. Mondanos. "Fracture hydromechanical response measured by fiber optic distributed acoustic sensing at milliHertz frequencies." *Geophys. Res. Lett. 44*, 2017, doi:10.1002/2017GL073931.

Becker, M. W., T. I. Coleman, and C. C. Ciervo. "Distributed Acoustic Sensing as a Distributed Hydraulic Sensor in Fractured Bedrock." *Water Resources Research, 56*, 2020, doi:10.1029/2020WR028140.

Berman, A. D., W. A. Ducker, and J. N. Israelachvili. "Origin and Charactrization of Different Stick-Slip Friction Mechnanisms." *Langmuir*, 1996, doi:10.1021/la950896z.

Bruno, M. S. "Use of Fiber Optic Distributed Acoustic Sensing for Measuring Hydraulic Connectivity for Geothermal Applications." Tech. rep., GeoMechanics Technologies, U.S. Department of Energy/Small Business Innovation Research, Bruno2018.

Bücker, C., and S. Grosswig. "Distributed temperature sensing in the oil and gas industry - insights and perspectives." *Oil Gas European Magazine* 43 (2017).

Cardarelli, F. "Ferrous Metals and Their Alloys." *In: Materials Handbook. Springer, Cham.*, 2018, doi:10.1007/978-3-319-38925-7_2.

Chang, H., and N. Nakata. "Investigation of the time-lapse changes with the DAS borehole data at the Brady geothermalfield using deconvolution interferometry." *SEG Technical Program Expanded Abstracts : 3417-3421*, 2020, doi:10.1190/segam2020-3426023.1.

Daley, T. M., D. E. Miller, K. Dodds, P. Cook, and B. M. Freifeld. "Field testing of modular borehole monitoring with simultaneous distributed acoustic sensing and geophone vertical seismic profiles at Citronelle, Alabama." *Geophysical Prospecting*, 2016, doi:10.1111/1365-2478.12324

Daley, T. M., et al. "Field testing of fiber-optic distributed acoustic sensing (DAS) for subsurface seismic monitoring." *The Leading Edge*, 2013, doi:10.1190/tle32060699.1

Finfer, D. C., V. Mahue, S. Shatalin, T. Parker, and M. Farhadiroushan. "Borehole Flow Monitoring using a Non-intrusive Passive Distributed Acoustic Sensing (DAS)." *Society of Petroleum Engineers*, 2014, doi:10.2118/170844-MS

Förster, A., J. Schrötter, D. F. Merriam, and D. D. Blackwell. "Application of optical-fiber temperature logging - an example in a sedimentary environment." *Geophysics* 62(4) (1997), doi:10.1190/1.1444211

Ghahfarokhi, P. K., T. Carr, L. Song, P. Shukla, and P. Pankaj. "Seismic Attributes Application for the Distributed Acoustic Sensing Data for the Marcellus Shale: New Insights to Cross-Stage Flow Communication." *Society of Petroleum Engineers*, 2018, doi:10.2118/189888-MS

Götz, J., S. Lüth, J. Henninges, and T. Reinsch. "Vertical seismic profiling using a daisy-chained deployment of fibre-optic cables in four wells simultaneously – Case study at the Ketzin carbon dioxide storage site." *Geophysical Prospecting*, 2018, doi:10.1111/1365-2478.12638

Harris, K., D. White, D. Melanson, C. Samson, and T. M. Daley. "Feasibility of time-lapse VSP monitoring at the Aquistore CO2 storage site using a distributed acoustic sensing system." *International Journal of Greenhouse Gas Control*, 2016, doi:10.1016/j.ijggc.2016.04.016

Hartog, A. H. "A Distributed Temperature Sensor Based on Liquid-Core Optical Fibers." *Journal of Lightwave Technology*, 1983, doi:10.1109/JLT.1983.1072146

Hartog, A. H., and G. Gamble. "Photonic distributed sensing." *Physics World*, 1991, doi:10.1088/2058-7058/4/3/30

Henninges, J., E. Huenges, and H. Burkhardt. "In situ thermal conductivity of gas-hydrate-bearing sediments of the Mallik 5L-38 well." *Journal of Geophysical Research* 110 (2005), doi:10.1029/2005JB003734

Henninges, J., E. Martuganova, M. Stiller, B. Norden, and C. M. Krawczyk. "Wireline distributed acoustic sensing allows 4.2 km deep vertical seismic profiling of the Rotliegend 150 °C geothermal reservoir in the North German Basin." *Solid Earth 12*, 2021, doi:10.5194/se-12-521-2021

Hidnert, P. "Thermal Expansion of Heat Resisting Alloys (nickel-chromium, Iron-chromium and Nickel Chromium-iron Alloys)." *Bureau of Standards Journal of Research*, 1931.

Hurtig, E., S. Grosswig, M. Jobmann, K. Kühn, and P. Marschall. "Fibre-optic temperature measurements in shallow boreholes: experimental application for fluid logging." *Geothermics* 23 (1994), doi:10.1016/0375-6505(94)90030-2

639 Johannessen, K., B. K. Drakeley, and M. Farhadiroushan. "Distributed Acoustic Sensing - A New Way of
640   Listening to Your Well/Reservoir." *Society of Petroleum Engineers*, 2012, doi:10.2118/149602-MS

641 Lee, C. H., and A. A. Polycarpou. "Static Friction Experiments and Verification of an Improved Elastic-Plastic
642   Model Including Roughness Effects." *Journal of Tribology*, 2007, doi:10.1115/1.2768074

643 Lipus, M. P., T. Reinsch, T. B. Weisenberger, S. Kragset, A. Stefánson, and S. G. Bogason. "Monitoring of a
644   reverse cement job in a high temperature geothermal environment." *Geothermal Energy*, 2021,
645   doi:10.1186/s40517-021-00187-y

646 Lipus, M., T. Reinsch, C. Schmidt-Hattenberger, J. Henninges, and M. Reich. "Gravel Pack Monitoring With a
647   Strain Sensing Fiber Optic Cable." *Oil Gas European Magazine 4*, 2018, doi:10.19225/181202

648 Martuganova, E., M. Stiller, K. Bauer, J. Henninges, and C. M. Krawczyk. "Cable reverberations during wireline
649   distributed acoustic sensing measurements: their nature and methods for elimination." *Geophys.*
650   *Prospect.*, 2021, doi:10.1111/1365-2478.13090

651 Masoudi, A., M. Balal, and T. P. Newson. "A distributed optical fibre dynamic strain sensor based on phase-
652   OTDR." *Meas. Sci. Technol. 24*, 2013, doi:10.1088/0957-0233/24/8/085204

653 Mateeva, A., et al. "Distributed acoustic sensing for reservoir monitoring with vertical seismic profiling."
654   *Geophysical Prospecting*, 2014, doi:10.1111/1365-2478.12116

655 Miller, D. E., et al. "DAS and DTS at Brady Hot Springs: Observations about Coupling and Coupled
656   Interpretations." *PROCEEDINGS, 43rd Workshop on Geothermal Reservoir EngineeringStanford*
657   *University, Stanford, California, February 12-14, 2018*. 2020.

658 Munn, J. D., T. J. Coleman, B. I. Parker, M. J. Mondanos, and A. Chalari. "Novel cable coupling technique for
659   improved shallow distributed acoustic sensor VSPs." *Journal of Applied Geophysics*, 2017,
660   doi:10.1016/j.jappgeo.2017.01.007

661 Muraki, M., E. Kinbara, and T. Konishi. "A laboratory simulation for stick-slip phenomena on the hydraulic
662   cylinder of a construction machine." *Tribology International*, 2003, doi:10.1016/S0301-
663   679X(03)00054-9

664 Naldrett, G., C. Cerrahoglu, and V. Mahue. "Production Monitoring Using Next-Generation Distributed Sensing
665   Systems." *Society of Petrophysicists and Well-Log Analysts*, 2018.

666 Pearce, J. G., et al. "High Resolution, Real-Time Casing Strain Imaging for Reservoir and Well Integrity
667   Monitoring: Demonstration of Monitoring Capability in a Field Installation." *SPE Annual Technical*
668   *Conference and Exhibition*, 2009.

669 Raab, T., T. Reinsch, S. R. Aldaz Cifuentes, and J. Henninges. "Real-Time Well-Integrity Monitoring Using
670   Fiber-Optic Distributed Acoustic Sensing." *Society of Petroleum Engineers*, 2019, doi:10.2118/195678-
671   PA

672 Reinsch, T., J. Henninges, and R. Ásmundsson. "Thermal, mechanical and chemical influences on the
673   performance of optical fibres for distributed temperature sensing in a hot geothermal well."
674   *Environmental Earth Science 70* (2013), doi:10.1007/s12665-013-2248-8

675 Reinsch, T., T. Thurley, and P. Jousset. "On the mechanical coupling of a fiber optic cable used for distributed
676   acoustic/vibration sensing applications—a theoretical consideration." *Measurement Science and*
677   *Technology*, 2017, doi:10.1088/1361-6501/aa8ba4

678 Schölderle, F., et al. "Monitoring Cold Water Injections for Reservoir Characterization using a Permanent Fibre
679   Optic Installation in a Geothermal Production Well in the Southern German Molasse Basin."
680   *Geothermal Energy (in review)*, 2021, doi:10.1186/s40517-021-00204-0

681 Storch, T., T. Grab, U. Gross, and S. Wagner. "VISUAL OBSERVATIONS INSIDE A GEOTHERMAL
682   THERMOSYPHON." *Heat Pipe Science and Technology, An International Journal 4* (2013): 217–226,
683   doi:10.1615/HeatPipeScieTech.2014011210

684 Sun, Y., Z. Xue, H. Park, T. Hashimoto, and Y. Zhang. "Optical Sensing of CO_2 Geological Storage Using
685   Distributed Fiber-Optic Sensor: From Laboratory to Field-Scale Demostrations." *Energy Fuels*, 2020,
686   doi:10.1021/acs.energyfuels.0c03925

687 ToolBox, The Engineering. "Elastic Properties and Young Modulus for some Materials." *The Engineering*
688   *ToolBox. Retrieved January 6, 2012.*, 2012.

689 Vaezi, Y., and M. van der Baan. "Comparison of the STA/LTA and power spectral density methods for
690   microseismic event detection." *Geophysical Journal International*, 2015, doi:10.1093/gji/ggv419

691 Zhang, Y., X. Lei, T. Hashimoto, and Z. Xue. "Towards retrieving distributed aquifer hydraulic parameters from
692   distributed strain sensing." *Journal of Geophysical Research Solid Earth*, 2020,
693   doi:10.1029/2020JB020056
694